THE ASTROPHYSICAL JOURNAL, 428:384–392, 1994 June 10

THE FAR-INFRARED PHOTOMETER ON THE INFRARED TELESCOPE IN SPACE

A. E. LANGE AND M. M. FREUND
Department of Physics, UC Berkeley, Berkeley, CA 94720

AND

S. SATO, T. HIRAO, T. MATSUMOTO, AND T. WATABE
Department of Physics, Nagoya University, Furocho, Chikusa-ku, Japan
Received 1993 March 23; accepted 1993 December 10

ABSTRACT

We describe the design and calibration of the Far-Infrared Photometer (FIRP), one of four focal plane instruments on the Infrared Telescope in Space (IRTS). The FIRP will provide absolute photometry in four bands centered at 150, 250, 400, and 700 μm with spectral resolution $\lambda/\Delta\lambda \approx 3$ and spatial resolution $\Delta\Theta = 0.5$ degrees. High sensitivity is achieved by using bolometric detectors operated at 300 mK in an AC bridge circuit. The closed-cycle ^{3}He refrigerator can be recycled in orbit. A 2 K shutter provides a zero reference for each field of view. More than 10% of the sky will be surveyed during the 3 week mission lifetime with a sensitivity of less than 10^{-13} W cm^{-2} sr^{-1} per 0.5 degree pixel.

Subject headings: artificial satellites, space probes — infrared: general — instrumentation: photometers

1. INTRODUCTION

The diffuse brightness of the sky has been mapped over most of the electromagnetic spectrum, from radio to gamma rays. The submillimeter region (wavelengths from 100 μm to 1 mm) is a particularly rich area of the spectrum, containing the Wien limit of the 2.74 K cosmic microwave background (CMB), the peak of thermal emission from interstellar dust (ISD), a rich spectrum of fine-structure and molecular transitions from the gas phase of the interstellar medium (ISM), and the long wavelength tail of emission from interplanetary dust (IPD). The brightness of the diffuse continuum emission at wavelengths of 300 to 500 μm is lower than any other portion of the spectrum between the UV and the radio. This spectral window coincides with the peak brightness of the diffuse background expected from distant, infrared-bright galaxies.

Measurements of the absolute brightness of the diffuse sub-mm continuum require a space-borne, liquid ^{4}He-cooled telescope with excellent sidelobe rejection and sensitive detectors. Several generations of rocket-borne intruments have measured the spectrum of the CMB (Gush, Halpern, & Wishnow 1990), the distribution of ISD emission (Kawada et al. 1994), and the line emission from the ISD (Bock et al. 1993). Recently the first comprehensive, all-sky view of the sub-mm background has been produced by the *Cosmic Background Explorer* (*COBE*) (Boggess et al. 1992). The FIRAS experiment on *COBE* has measured the spectrum of emission over the entire sky at wavelengths between 100 μm and 1 cm with 7 degree angular resolution, confirming the blackbody spectrum of the CMB (Mather et al. 1990), measuring the average spectrum of ISD emission, and detecting several lines emitted by the diffuse ISM (Wright et al. 1991). The DIRBE experiment has mapped the sky with finer resolution (0.7 degrees) in two sub-mm passbands, centered at 150 and 250 μm (Hauser et al. 1991).

This paper describes the Far-Infrared Photometer (FIRP), a multichannel absolute photometer with four passbands centered at 150, 250, 400, and 700 μm. The FIRP is one of four focal plane instruments on the Infrared telescope in Space (IRTS) (Murakami et al. 1994). The 15 cm, liquid ^{4}He-cooled telescope (Onaka et al. 1994) provides a $0\overset{\circ}{.}5$ field of view for the FIRP, which is diffraction limited at a wavelength of 1 mm. Approximately 10% of the sky will be surveyed during the 3 week mission. Other instruments include a Near-Infrared Spectrometer (NIRS) (Noda et al. 1994), a Mid-Infrared Spectrometer (MIRS) (Roellig et al. 1994), and a Far-Infrared Line Mapper (FILM) (Shibai et al. 1994).

2. FIRP SCIENCE GOALS

Coverage over the entire sub-millimeter band with high sensitivity and 0.5 degree spatial resolution makes the FIRP ideal for studying continuum emission from ISD, and for probing the cosmological "window" at 300–500 μm. The FIRP observations will complement both the FIRAS and the DIRBE observations by providing higher angular resolution than FIRAS, and by extending the DIRBE observations to longer wavelengths and higher sensitivity.

2.1. *Temperature Distribution of the ISD*

The sky-averaged spectrum of the diffuse sub-millimeter continuum background measured by FIRAS is dominated by the CMB at wavelengths greater than 500 μm, and by emission from ISD at wavelengths of 100 to 500 μm. When the spectrum of the CMB is removed, the residual spectrum is best fit by a two-temperature model of the form (Wright et al. 1991):

$$I(\nu)\alpha\nu^2\{B_\nu(20.4K) + 6.7B_\nu(4.77)\}\,,$$

where $B_\nu(T)$ is the Planck function and the ν^2 dependence describes the scaling of emissivity with frequency expected for emitters that are small in comparison with the wavelength of emission. That this two component model formally fits the data better than a single component model suggests the existence of a population of interstellar dust grains that are efficient long wave emitters, such as conducting needles or fractal dust grains (Wright 1987). The observed spectrum of ISD emission could result either from a mixture of two populations of ISD that equilibrate at different temperatures, or from the existence of efficient long-wave emitters that have a heat capacity sufficiently small that absorption of a single UV photon heats them significantly. In the latter case, the observed "two-component" spectrum could be an artifact resulting from a homogeneous population of dust emitting over a range in temperature. In either case, the spectrum of the ISD emission should exhibit spatial variation due to the variation in dust grain properties and/or incident radiation field. Sub-mm measurements at higher angular resolution probe this variation with greater sensitivity, and should, when combined with other probes of the ISM, provide clues to the detailed nature of the ISD emission. DIRBE provides limited information on this aspect of ISD emission. Its spectral coverage extends only to 300 μm, and thus misses the region of the spectrum from 300 μm to 1 mm where emission from the "cold component" should be observable. In addition, the sensitivity of the DIRBE sub-mm channels at 150 and 250 μm provides only modest signal-to-noise at high Galactic latitudes.

2.2. *Anisotropy of the Cosmic Background Radiation*

Though the FIRP beam size is matched to the angular scales on which standard cold dark matter scenarios predict that the temperature anisotropy of the CMB will peak (Bond 1989), the confusion from ISD at sub-mm wavelengths will prevent the FIRP from reaching interesting limits. Several experiments have been designed and are now operating which attempt to measure the anisotropy of the CMB at mm wavelengths on these angular scales (Fischer et al. 1992). Confusion by ISD emission will ultimately limit the sensitivity of measurements of CMB anisotropy at wavelengths of 1 to 3 mm (Fischer et al. 1994). Attempts to model this emission using high signal-to-noise data available from *IRAS* and DIRBE at wavelengths ≤ 100 μm may be confounded by spatial inhomogeneities in the temperature and/or spectral index of the dust, since these measurements are made in the Wien limit of the dust spectrum, and must be extrapolated over a decade of frequency.

Observations of ISD emission with the FIRP at wavelengths adjacent to those at which CMB anisotropy observations are conducted, will improve the precision with which mm-wavelength ISD emission can be modeled and subtracted from CMB anisotropy measurements.

2.3. *The Extragalactic Submillimeter Background*

Measurements of the diffuse electromagnetic background probe all radiative processes in the universe over a volume which depends on the absorption depth for radiation. For sub-mm measurements, this volume includes the entire universe back to the last scattering surface of the CMB at $z = 1000$, in the standard scenario in which the reionization occurs at $z < 4$. The sub-mm background thus contains the integrated light from all radiative processes that have taken place in the postrecombination universe at wavelengths of $(100\text{–}1000)/(1 + z)$ μm, where z is the redshift of emission. The sub-mm extragalactic background is thought to be dominated by emission from distant, infrared bright galaxies (Beichman & Helou 1990; Wang 1991). The brightness and spectrum of the sub-mm extragalactic background depends on the rate of star formation as a function of redshift, and on the dust opacity along the line of sight. For high dust opacity, most of the starlight emitted at high redshift will be absorbed and reradiated in the infrared, and will appear in the sub-mm. For low dust opacity, the optical depth to starlight emitted at high redshift will be small, and the starlight will appear in the near-infrared.

The extragalactic infrared background has yet to be reliably detected at any wavelength. Observations to date have shown that the diffuse background over most of the sky is dominated by foreground emission from the Galaxy and the Solar System through the infrared. Accurate modeling of the spectrum and spatial distribution of these "local" sources of emission is necessary in order to detect an isotropic extragalactic backgound. Emission from ISD is the dominant source of foreground emission in the sub-mm. This emission decreases rapidly at long wavelengths, creating a deep spectral window at 300 to 500 μm between the ISD emission and the CMB through which the infrared emission from distant galaxies may be observable. Another window at 3 to 5 μm, between the scattered sunlight and the thermal emission from the interplanetary dust, provides the best hope of observing the near-infrared background due to redshifted starlight. These two windows are targeted by the FIRP and the NIRS, respectively, which will have overlapping sky coverage.

The sensitivity and spatial resolution of the FIRP will allow the diffuse background to be mapped with good signal-to-noise in the dimmest regions of the sky. The wavelength coverage extends to 800 μm, and includes a passband tailored to the 300 to 500 μm spectral window. This data set, in addition to the data from the NIRS, MIRS, and FILM should significantly improve models of the local backgrounds based on the all-sky coverage of the DIRBE and FIRAS experiments on *COBE*, allowing a more accurate determination of the isotropic extragalactic background.

3. THE IRTS MISSION

The IRTS is one of ten experiments that will be placed into orbit on the first Space Flyer Unit (SFU-1), which is scheduled for launch from Tanegashima Space Center in early 1995. The SFU will be placed into a nearly circular, 482 km altitude, 28.5 degree inclination orbit. The entire IRTS experiment, including the warm electronics, has a mass of 183 kg, and a volume of approximately 3 m^3.

After a nominal seven day checkout and degassing period in orbit, the IRTS aperture cover will be ejected, and observations with all four instruments will begin. The SFU mission will be dedicated to IRTS observations for the next 20 days. During this period the SFU attitude will be determined by the Earth and Sun avoidance requirements of the IRTS, and all other experiments on the SFU will be powered down in order to eliminate potential interference with the sensitive IRTS electronics. Present tests of the flight cryostat indicate that the superfluid ^{4}He hold time will be more than adequate to last through the observation period. After a period of 6–18 months after launch, the SFU-1 is scheduled to be retrieved from orbit by NASA's Space Transportation Systen for refurbishment in the future.

The scan pattern of the IRTS telescope is determined by Earth and Sun avoidance requirements, and the low-inclination orbit (Murakami et al. 1994). The scan keeps the sun more than 70° from the optical axis at all times, and the Earth's limb more than 93° from the optical axis in the best orbits, and more than 43° from the optical axis in the worst orbits. The optical axis of the telescope will sweep a great circle on the sky once per orbit, the plane of the circle inclined 20 degrees to the Earth-Sun axis. Sky coverage will thus include solar elongation angles of 70 to 110 degrees. The scan rate will be 0.067 degrees s^{-1}, or 8 s per field of view for the FIRP. The axis of the great circle scan will be precessed at a rate of 360 degress yr^{-1}, or 0.067 degrees per orbit. The FIRP will thus observe point sources on eight or more consecutive orbits, the redundant coverage being minimal in the plane of the ecliptic, and maximum near the ecliptic poles. Approximately 10% of the sky will be observed in the anticipated 21 day mission.

The IRTS telescope is of Ritchey-Chretien design with gold-coated aluminum optics (Onaka et al. 1994). The system of baffles employs a combination of sunshade, passively cooled aperture shield, cryogenically cooled specular forebaffle, and black aftbaffle (Bock et al. 1994). The specular forebaffle reflects radiation incident more than 40 degrees off axis out of the telescope, keeping the aperture heat load below 20 mW for Earth-avoidance angles of more than 40 degrees. The telescope is surrounded by a 100 liter liquid ^{4}He cryostat, which is pumped through a porous plug to the vacuum of space to a temperature of less than 1.8 K. The aftbaffle and the telescope optics are thermally coupled directly to the ^{4}He tank, and are cooled to less than 2 K. The forebaffle is cooled to less than 19 K by heat exchange with the venting ^{4}He gas in the least favorable orbits, and can be cooled to less than 2.5 K via a gas-gap heat switch that thermally grounds the forebaffle to the ^{4}He tank during more favorable orbits, when the Earth limb remains more than 58 degrees off-axis.

Data from all four of the focal plane instruments, a focal plane star-sensor, and telescope housekeeping are multiplexed into a 6 kb s^{-1} common telemetry stream, and stored in the spacecraft's 80 Mbit bubble memory. The data are telemetered to the ground during brief downlinks as the spacecraft passes over receiving stations in NASA's Deep Space Network and Japan's Kagoshima Space Center. After recording and on-site archiving, the data will be transmitted to the IRTS Science Operations Center at the Institute for Space and Astronautical Science in Japan for processing. The entire IRTS data set will eventually be made available to the public through the Image Processing and Analysis Center (IPAC) in the United States.

4. FIRP INSTRUMENT DESCRIPTION

The modest scale of the IRTS mission presented all of the focal plane instruments with severe constraints in size, mass, power dissipation, complexity, and data rate. Since all four focal plane instruments are intended to be operated simultaneously, it was important to eliminate all sources of optical, electrical, thermal, and mechanical interference between the instruments. As the IRTS facility does not provide infrared calibration sources, each instrument must incorporate its own. To meet the FIRP science goals within these constraints, a simple optical system based on a four-channel photometer was chosen. The design of the FIRP is illustrated in Figures 1*a* and 1*b*. A closed-cycle ^{3}He refrigerator that can be recycled in orbit was developed to provide a 0.3 K heat sink for the bolometric detectors. A novel bolometric detector system was developed that eliminates the need for rapid signal modulation via a mechanical chopper. The only moving part in the instrument is a 2 K shutter that provides a zero reference. The most important specifications and performance characteristics of the FIRP are given in Table 1. A more detailed description of the instrument is given below.

4.1. *Optical Components*

The IRTS focal plane is divided among the science instruments and a near infrared star sensor by a set of pick-off mirrors. The FIRP feed optic, a compound parabolic concentrator (Winston 1970), occupies the center of the focal plane, and defines a 0.5 degree FWHM field of view. The acceptance angle of the FIRP is matched to the f/4 beam at the focal plane. The entrance apertures of the NIRS, FIRP, and MIRS are

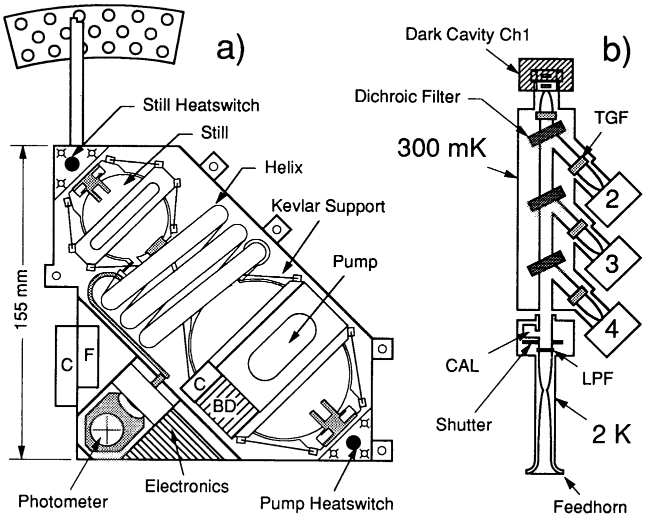

FIG. 1.—(*a*) FIRP, viewed from top along the optical axis of the telescope. The photometer and the refrigerator are optically isolated from each other. Two gas-gap heat switches are used to cycle the ^{3}He refrigerator in zero-g. Kevlar suspension systems thermally isolate the pump, still, and photometer from the 2 K housing. The Cu cold strap minimizes thermal gradients between the FIRP and the ^{4}He cryostat. A burst disk "BD" attached to the refrigerator prevents overpressure. The cold electronics consist of four dual JFET amplifiers. Electrical connection to the refrigerator and to the photometer is made separately via two connectors "C" with integrated two-pole LC low-pass and Eccosorb (Emmerson Cuming) filters "F" for RF-noise protection. (*b*) Schematic of the FIRP optical path. After the 2 K feed optic the beam passes the primary low-pass filter (LPF), the shutter, and the calibration lamp cavity (CAL), before entering the 300 mK photometer. The beam propagates via light pipe inside the photometer. Three dichroics separate the incoming beam into four passbands, labeled by wavelength. Thick-grill filters (TGF) provide additional high-pass filtering for each band. Radiation from each band is concentrated into an integrating cavity containing a composite bolometric detector. A second, matched detector is located in an adjacent dark cavity. The two detectors are operated in an AC bridge.

TABLE 1

FIRP SPECIFICATIONS

Parameter	Value
Size (cm)	Irregular shape: 16 × 15 × 11 overall
Weight (g)	≈2185
Electrical Power Dissipation:	
Cold part (mW)	2–3 typical, 17 peak
Warm part (W)	≈2
Cryogenic Parameters:	
$T_{\rm coldplate}$ (K)	<1.8
$T_{\rm housing}$ (K)	1.92
$T_{\rm telescope}$ (K)	1.91
$T_{\rm still}$ (mK)	≈293
$T_{\rm phot}$ (mK)	≈319
$T_{\rm pump}$ (K)	≈2.1
^{3}He lifetime (days)	≈10
^{3}He cycle time (hr)	≈15
Cooling power of still (J)	≈12
Heat load (on still) (μW)	≈14.6
Entrance aperture	4 mm diameter (0°5 on sky) Winston Concentrator with flare entrance aperture
Detectors	Composite bolometers in AC bridge with dark reference detectors
Shutter frequency (Hz)	1/8 (4 s open/4 s closed—8 s per FOV)
Cold amplifiers	Model J-1, Infrared Laboratories
Data rate:	
Standard (kb s^{-1})	6
Reduced (kb s^{-1})	3

collinear along the scan direction of the telescope. The entrance apertures of the FILM, FIRP, and star sensor are collinear perpendicular to the scan direction.

The optical path of the FIRP is shown in Figure 1*b*. The entrance aperture of the FIRP feed optic is smoothly flared with a 2 mm constant radius of curvature in order to reduce diffraction. A second compound parabolic reflector placed at the exit aperture of the feed optic recollimates the beam to f/2.8 into light-pipe optics before it enters the instrument.

The beam first passes through a Yoshinga-type filter (Yamada, Mitsuishi, & Yoshinaga 1962) with a low-pass cutoff at 100 cm^{-1}. The filter is identical to that used previously in rocket-borne measurements of the sub-mm background (Lange et al. 1987), and has been confirmed to have high out-of-band rejection throughout the infrared. The filter forms the high-frequency edge of the 150 μm passband, and provides additional out-of-band blocking for the other passbands.

After passing the shutter, described below, the beam enters the 300 mK photometer which houses the dichroic beam splitters, out-of-band blocking filters, and bolometric detectors. The 300 mK photometer is thermally isolated from the 2 K shutter module by a 300 μm gap in the 4 mm diameter light pipe. The photometer is held rigidly in place via an 8 point Kevlar suspension system (Duband, Hui, & Lange 1993).

Each of the three dichroic beamsplitters is a multilayer capacitive-mesh low-pass filter used at 22.5 degrees angle of incidence (Ade et al. 1984). The half-power points of the three dichroics are at 200, 350, and 600 μm. The beam is incident on the dichroic filters in order of decreasing cutoff frequency, separating off the passbands in order of decreasing frequency. This ordering provides additional blocking of high-frequency out-of-band leaks for the lowest frequency channels. The long wavelength edge of the three shortest wavelength passbands is formed by the reflection spectrum of the dichroics, which drops to less than 3% in-band. The in-band transmission of the dichroics is high ($\approx$80%) so that the loss incurred by transmission through several dichroics is small.

After emerging from the system of dichroics, each beam passes through a thick-grill filter (Timusk & Richards 1981) which provides low-frequency blocking, and is then concentrated into an integrating cavity by an f/2.8 compound parabolic reflector. The thick-grill filter in the 700 μm channel forms the long-wavelength edge of the band and has cutoff at 850 μm. The thick grill filters in the other three channels are used to improve the long-wavelength blocking in the region where the CMB spectrum is steeply rising, and they have identical half-power points at 475 μm.

4.2. *Shutter*

The shutter is located immediately behind the low-pass filter. In normal operation, the shutter modulates the beam at 1/8 Hz in a square wave with 4 s open and 4 s closed, providing a zero-reference for each field of view. The large number of duty cycles, the strict limits on power dissipation, and the acoustic sensitivity of bolometric detectors required a novel design. The shutter that we have developed is a modification of a shutter developed for the Long-Wave Spectrometer on ISO. The blade is mounted on a flex pivot, along with two SmCo permanent magnets. Two solenoids with soft iron cores are positioned such that the combination of the spring force due to the flex pivot, and the magnetic force between the permanent magnets and the solenoid cores creates a potential with two stable minima corresponding to the open and closed positions of the shutter. When the solenoids are energized, the permanent magnets are repulsed from one pole piece and attracted toward the other, temporarily creating a potential with a single stable position.

In order to cycle the shutter between open and closed, the solenoids are energized for 50 ms with approximately 10 mA of current, alternating the polarity of the pulse every 4 s. The absence of hard stops makes the motion acoustically quiet. Oscillation of the shutter blade in the magnetic potential is damped by Eddy current damping induced in the high-purity copper blade by two small SmCo magnets placed beneath the blade. The switching time is less than 100 ms, shorter than the time constant of the bolometric detectors. After each shutter operation, a transient in the signal in the lowest frequency channel is observed, due to heating of the shutter blade by the Eddy current damping. This transient decays with a 300 ms time constant, and is approximately symmetric with respect to the shutter opening and closing. The response to the transient is thus subtracted to first order in the signal processing, described below, which differences the average signal observed during the shutter open and closed phases.

4.3. *Detectors*

The FIRP achieves high sensitivity by using low-background, long time-constant bolometric detectors cooled to 0.3 K. The details of bolometer theory have been described by Mather (1984). The FIRP bolometers have been described by Devlin et al. (1991). An infrared absorber with a heat capacity C is thermally isolated from a heat sink of temperature T_0 by a link with a thermal conductivity G. The power P incident on the absorber induces a temperature difference $(T - T_0) = P/G$. The absorber temperature responds to changes in the power with a time constant $\tau = C/G$. A thermistor is attached to the absorber, and measures the temperature. The FIRP bolometers at 300 mK have a thermal conductivity $G = 1.5 \times 10^{-10}$ W K^{-1}, a heat capacity $C = 10^{-11}$ J K^{-1}, and a time constant $\tau = 150$ ms. The measured electrical noise equivalent power (NEP) of each detector is $\approx 2 \times 10^{-17}$ W $\mathrm{Hz}^{-1/2}$.

The bolometers are biased in an unconventional manner that reduces 1/f noise. Each illuminated detector is paired with a thermally matched dark detector in the bridge circuit shown in Figure 2. The bridge is biased with a square-wave AC voltage between 73 and 215 Hz, depending on the channel, producing a carrier frequency that is well above the 1/f knee of the amplifier. The output of the bridge is amplified by a cold J-FET source follower, and then differentially amplified by warm electronics, producing an AC signal that has an amplitude proportional to the infrared power absorbed in the active detector. The AC signal is phase-synchronously demodulated and integrated before digital sampling at 8 Hz. The AC bridge readout is described in detail by Wilbanks et al. (1990).

Differencing the signal between detectors with matched thermal response reduces 1/f noise due to fluctuations in the heat sink temperature. Using the AC bias eliminates contributions from 1/f noise in the amplifier chain. The reduction in 1/f noise allows signal modulation at low frequency, thus eliminating the need for a chopper and allowing slower, and thus more sensitive, detectors to be used. The FIRP signal modulation is accomplished by operating the cold shutter at 1/8 Hz.

4.4. ^{3}He *Refrigerator*

The ^{3}He refrigerator provides the 300 mK base temperature needed for the operation of the FIRP detectors. The three main requirements for the FIRP ^{3}He refrigerator are (i) the ability to

1994ApJ...428..384L

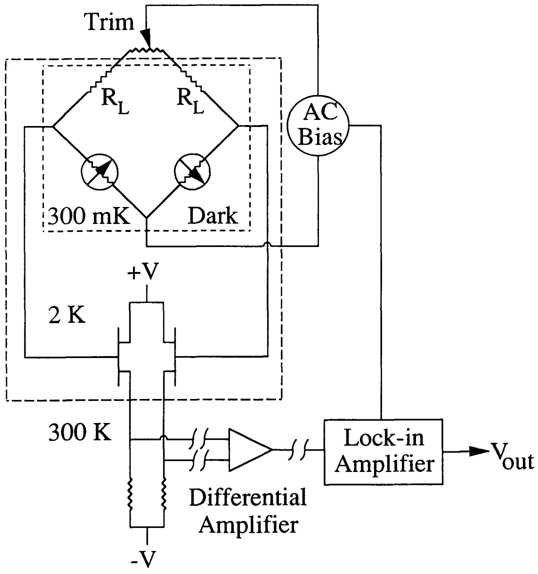

FIG. 2.—Schematic of the AC bridge readout used for the bolometric detectors. R_L = 10.0 MΩ denote the load resistors.

condense ^{3}He and operate in zero-g with minimal heating of the focal plane, (ii) a long hold time and high duty cycle in orbit, and (iii) a self-contained and compact design that requires no mechanical penetration of the instrument cavity. A detailed description of the design of the FIRP refrigerator is given by Duband, Hui, & Lange (1990b). A prototype refrigerator (Duband et al. 1990a) has been tested on a sounding rocket, verifying the performance in zero-g (Duband et al. 1991).

The FIRP refrigerator has five major components, as shown in Figure 1*a*: an evaporator, a helical pump tube, a sorption pump, and two heat switches. The evaporator holds the ^{3}He liquid during normal operation. It is filled with a silicose sponge, which contains the liquid ^{3}He in the still by surface tension. A thin-walled, stainless-steel helical pump tube connects the evaporator to the sorption pump, and provides a large ratio of pumping speed to thermal isolation. The sorption pump is filled with activated charcoal, which adsorbs ^{3}He gas at low temperatures and releases the gas at temperatures greater than 15 K. The still and the pump are each separately suspended in Kevlar harnesses (Duband et al. 1993). Thermal contact to each can be made via gas-gap heat switches that have switching ratios of $\approx$2000 (Duband et al. 1990b). The refrigerator is charged with 16.8 liter-STP of ^{3}He. The room temperature pressure is 68 bar. A burst disk limits the maximum operating pressure to 110 bar.

Operation of the ^{3}He refrigerator is initiated after all of the components have been cooled to 2 K and the ^{3}He gas is absorbed in the pump. Liquid ^{3}He is condensed in the evaporator by thermally grounding the evaporator to the 2 K heat sink via the heat switch, and heating the pump to desorb the ^{3}He gas. The evaporator is the coldest point in the system at this point, ensuring that liquid condenses in it. A full cycle, which condenses 95% of the gas, requires heating the pump to 40 K. The speed of condensation is limited by the thermal contact with the 2 K heat sink. A full condensation requires 16 hours, during which 27 mW of power is applied to the pump, 10 mW flows to the 2 K heat sink, and the remainder is stored in the heat of condensation of the liquid.

In the second part of the cycle, the evaporator is thermally isolated, and the pump is thermally grounded to the 2 K heat sink. Absorption of ^{3}He gas in the pump reduces the vapor pressure in the evaporator, cooling it to $\approx$290 mK. The operating time between recycles is determined by the efficiency of condensation and by the heat load, both of which are functions of the heat sink temperature. With a 2 K heat sink, a total heat load of 15.1 μW is due to conduction through the evaporator heat switch (7.5 μW), the helical pump tube (3.1 μW), the Kevlar suspension of the evaporator, the photometer (0.5 μW), and electrical leads (4 μW). Figure 3 depicts the dependence of the lifetime of the still as function of both the condensation temperature ($T_{\rm still}$) and the housing temperature ($T_{\rm housing}$). For the operating conditions anticipated in orbit, the expected hold time of the refrigerator is greater than 10 days, giving a duty cycle efficiency of more than 90%.

In order to achieve this efficiency, it is essential to provide good thermal contact between the FIRP and the liquid ^{4}He in the IRTS cryostat. A high purity Cu heat strap connects the Cu base of the evaporator heat switch and the FIRP housing directly to the Al ^{4}He tank. The strap is 0.4 cm^2 × 15 cm, and attaches to a 21 cm^2 flange on the cryostat with 15 M3 screws. Electrical isolation of the FIRP from the cryostat is accomplished by a Cu-epoxy-Cu sandwich at the flange using Stycast epoxy (Emmerson Cuming) that has a thermal conductivity at 2 K of 350 mW K^{-1}. The thermal conductivity between the evaporator and the liquid ^{4}He is dominated by the Al cryostat itself, and is of the order of about 100 mW K^{-1}. A complete list of operating parameters of the FIRP ^{3}He refrigerator is included in Table 1.

4.5. *Thermometry*

The FIRP housekeeping continuously monitors temperatures at five positions: the photometer, the still, the pump, the shutter module, and the telescope primary. The pump thermometer is a Si diode. The photometer, still, and telescope primary thermometers are Ge resistance thermometers. The shutter thermometer is a carbon resistor. Zero offsets are checked at 256 second intervals by nulling the bias currents for all thermometers (except the photometer thermometer) for one second. In addition to the FIRP housekeeping, the IRTS

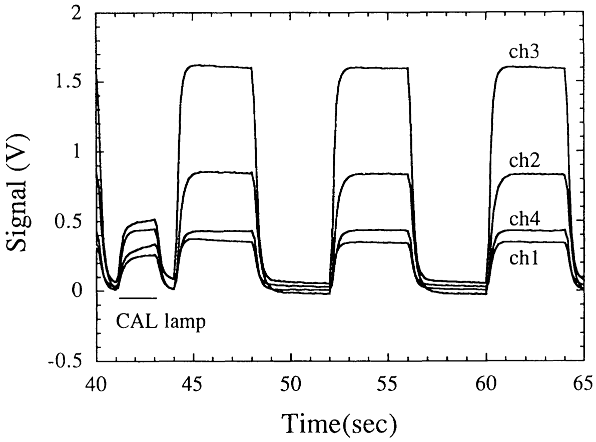

FIG. 3.—Calculated lifetime of the ^{3}He refrigerator as a function of housing temperature during operation and condensation temperature (2.0, 2.2, and 2.4 K). The housing temperature and the condensation temperature predicted for flight are between 1.7 and 1.85 K and 2.2 and 2.3 K, respectively, yielding a lifetime of the ^{3}He refrigerator of between 9.5 and 11 days.

1994ApJ...428..384L

system housekeeping monitors a variety of temperatures in the telescope, baffle system, cryostat, and electronics.

4.6. *Internal Calibration Source*

The primary calibration of the FIRP will be provided by observing bright regions of the sky that will have already been mapped by the DIRBE at similar angular resolution with good signal-to-noise in the two shortest wavelength channels. Extrapolations of the brightness of these regions to longer wavelengths using the FIRAS and balloon-borne data (Fischer et al. 1994) will be used to calibrate the longer wavelength channels. These primary calibrations will be frequent, since the scan path will cross the Galactic plane twice each orbit.

In order to measure the gain stability more frequently, two internal calibrator lamps are activated every 256 seconds. The lamps consist of doped Ge thermistors, mounted on 1 mil (25 μm) brass wires, and suspended in a cavity. The cavity is connected to the light pipe by a 0.8 mm hole just behind the shutter and primary Yoshinga filter. During the calibration sequence, the lamps are activated for 2 seconds with a constant current bias in the middle of an extended shutter close, which lasts 10 seconds. Electro-thermal feedback quickly stabilizes the temperature of the calibrator lamps at approximately 20 K, providing a signal to noise of several hundred in the four channels.

4.7. *Electronics*

Cold JFET amplifiers positioned a few cm from the photometer are used as the first stage of the differential amplifier for each AC bridge circuit. The JFET amplifiers are heat sunk to the 2 K instrument housing. A total power dissipation of 500 μW per JFET pair maintains the device at approximately 65 K, for optimum noise performance. The JFET amplifiers are operated as source followers, providing unity voltage gain, and with an output impedance of approximately 4 kΩ.

The FIRP warm electronics is mounted on a single board. It consists of an analog part, which handles all the signals to and from the cold FIRP, the star sensor, and the telescope thermometer, and a digital part which interfaces with the IRTS common board and the IRTS data processing unit (DPU). The analog part provides the bias signals for the different FIRP channels and the photometer thermometer. The FIRP board generates six bias frequencies between 73 and 215 Hz that were chosen to minimize cross talk and sensitivity to external noise sources. The signal from the cold JFET source followers (one for each detector) is preamplified and phase-synchronously demodulated. The total gain of the amplifier chain is 56,000.

4.8. *Data Acquisition and Signal Processing*

The FIRP telemetry stream is interwoven with that of the other focal plane instruments and the housekeeping data. The DC analog output of each detector bridge is low-pass filtered by a two-pole filter with a cutoff at 2 Hz, and sampled at 8 Hz by a 16 bit A/D converter. The sampling rate for the thermometers is 2 Hz.

Figure 4 shows the digitally sampled output of the four detector channels during a calibration experiment in which the instrument is viewing a source which has brightness typical of the brighter regions of the sky. The modulation of the signal by the shutter at 1/8 Hz is apparent, as well as the response to the internal calibrator when the shutter is closed. There are 64 samples for each shutter period. We compute the average signal for the nth shutter cycle, $\langle S_n \rangle$, as the difference

$$\langle S_n \rangle = \langle S_{\mathrm{open},n} \rangle - 1/2\{\langle S_{\mathrm{closed},n-1} \rangle + \langle S_{\mathrm{closed},n} \rangle\} .$$

This is the quantity that we are normally interested in, since the 8 s shutter period corresponds with the length of time required for the beam to move one diameter on the sky. In forming the signal averages for the shutter open and close periods, we normally delete several samples immediately following the shutter transient.

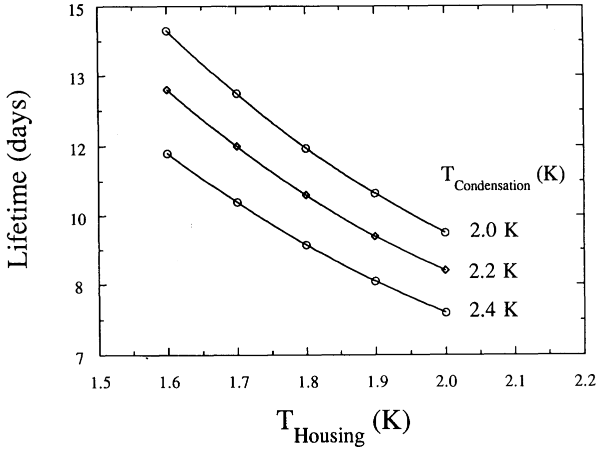

FIG. 4.—Digitally sampled signal output while the instrument views a 20 K blackbody source through a 1% neutral density filter. The signal at the left during the period when the shutter is closed is due to the calibration lamp. In the normal flight calibration sequence, the calibration lamp is activated for 2 seconds every 256 seconds in the middle of a 10 second shutter closing.

5. LABORATORY PERFORMANCE AND CALIBRATION

The FIRP was tested and calibrated extensively in the laboratory prior to delivery to the flight cryostat. The testing and calibration proceeded in three phases: (1) spectroscopy of the flight filter system using a Michelson interferometer (2) initial testing and calibration of the fully assembled instrument in a small test cryostat that contained the FIRP and a small blackbody calibration source that filled the field of view of the feedhorn, and (3) installation of the FIRP on the flight focal plane with the three other focal plane instruments, the star sensor, and the flight telescope, and calibration using a large blackbody calibrator.

5.1. *Spectroscopy*

The low-background flight detectors were unsuitable for measuring the spectral response of the instrument in the laboratory. The spectral response was measured prior to integrating the photometer into the flight housing, using high-background composite bolometric detectors with absorbing substrates identical to those used in the flight detectors. The bolometers were operated in a conventional AC-coupled, DC-biased readout to facilitate the measurements. The photometer and shutter module were installed in a small test cryostat that provided a 0.3 K cold stage for the photometer, and a 2 K cold stage for the shutter module containing the primary low-pass filter. All of the filters were thus at their normal operating temperature during the measurement.

The spectral response was measured using a step-and-integrate Fourier Transform Spectrometer, which keeps the signal modulation independent of wavelength, and thus eliminates effects due to finite detector time constants. The flight filter system viewed the spectrometer through a black polyethylene filter mounted on a LN$_2$ radiation shield, and a 1 mil polypropylene vacuum window at room temperature. Neither of these materials has any significant spectral features at sub-mm wavelengths. The output of the spectrometer was normalized by using a second detector which viewed the spectrometer through separate, but identical, black polyethylene and polypropylene filters. The second detector was a composite bolometer (Lange et al. 1983) which accepted a larger throughput, corresponding to a long wavelength cutoff of 2 mm.

The measured spectral response for the four passbands are shown in Figure 5. The spectral response should be independent of the specific bolometric detectors used, since the absorbing substrates of the composite bolometric detectors are tailored to have frequency-independent absorption. This independence is confirmed by the laboratory calibration described below.

No evidence of out-of-band leaks from ≈ 50 μm to 3 mm was observed in the spectroscopy, to a level of less than 0.1% of the peak transmission. More stringent limits on the out-of-band response can be placed by separate measurements of the individual components. The transmission spectrum of the primary low-pass filter has been measured at wavelengths of 1 μm to 1 mm, and found to provide blocking throughout the infrared adequate to make the out-of-band response to the steeply rising spectrum of zodiacal light negligible in comparison with in-band response, even in the regions of the sky where ISD emission is dimmest. In addition, visible light measurements confirmed a high level of short-wavelength rejection in the three longer wavelength channels by the dichroic filters. The measured response to a visible light source illuminating the entrance of the room temperature photometer was measured by placing a photodiode at the position of the 250, 400, and 700 μm detectors, and found to be 3×10^{-3}, 2×10^{-5}, and 10^{-7}, respectively.

5.2. *Calibration*

The responsivity of each channel was measured in several configurations using blackbody calibrators at temperatures between 1.6 and 30 K. In principle, only two blackbody temperatures are necessary in order to calibrate the gain and zero-offset of each channel. Measuring the response to a number of blackbody temperatures over a large range of temperature thus provides a powerful test for systematic errors in the calibration. For each blackbody temperature T, the power in each passband is calculated by convolving the measured spectral response with the Planck function $B_\nu(T)$. The measured response, normalized to the response to the calibrator lamps to correct for time-variations in the instrument gain, should be linearly related to the in-band power. Any errors in the spectroscopy or the blackbody thermometry, or nonlinearities in the detector response, will be apparent as a deviation from linearity in the plot of response versus power. Particularly stringent tests of the spectroscopy are made when the measured data includes temperatures which place the peak of the Planck function on either side of the passband.

The calibration was carried out in two environments. In the first, the FIRP was installed in a cryostat with a small blackbody that filled the field of view of the feedhorn. Two types of calibration experiment were performed in this configuration. In one, the blackbody was viewed directly over a temperature range of 1.6 to 8 K. In another the blackbody was viewed through a 1% neutral density filter over a temperature range of 4 to 30 K. The overlap in temperature range of the two configurations confirmed the transmittance of the neutral density filter. Figure 6 shows the calibration data for the 400 μm channel for the blackbody calibration from 2.70 to 7.00 K. The derived responsivity is constant to within 3% over this temperature range. Figure 7 shows a histogram of $\langle S_n \rangle$ for $T = 1.6$ K. The measured variance in $\langle S_n \rangle$ is 4 nV. The mean value, which corresponds to an instrumental zero-offset that is not removed by the shutter modulation, is -0.7 nV. The typical amount of integration time per field of view will allow us to integrate down to a 1 σ noise level of approximately 2 nV.

The second experiment was conducted in a large test cryostat in which the flight telescope and all of the focal plane instruments were installed. A large blackbody cavity was installed just above the secondary shroud that contained a variable temperature blackbody, and had four exit apertures 4 mm in diameter, equally spaced around a 100 mm diameter circle in the face above the primary mirror. The holes were oriented so that the focal plane would view them without obscuration by the secondary spiders. The copper walls of the cavity were maintained at close to 2 K, and the outside of the front surface, which was viewed by the focal plane, was painted

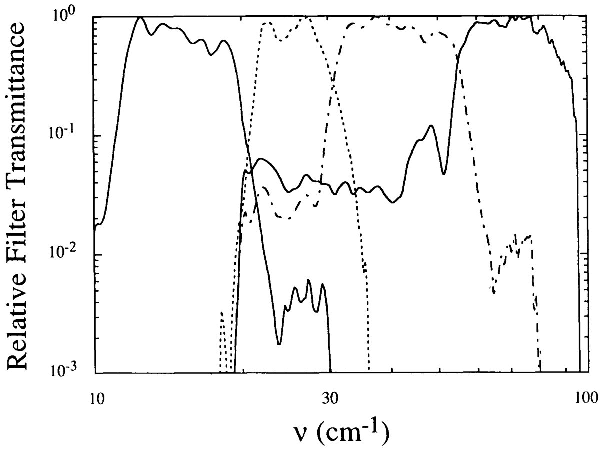

FIG. 5.—Measured spectral response of the four passbands. Note the low-frequency leakage in the two highest frequency channels (3 and 4).

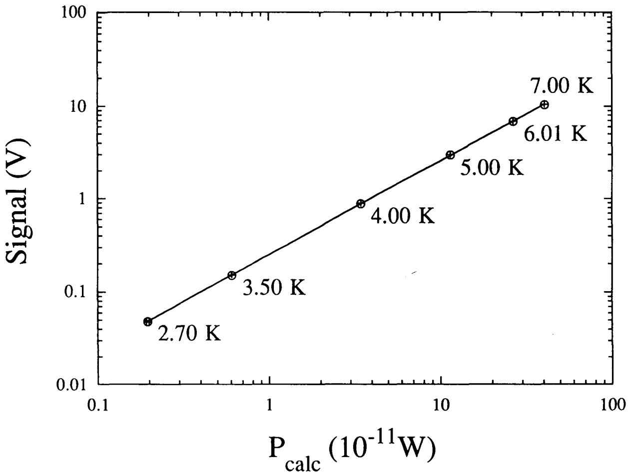

FIG. 6.—Result of the primary calibration experiment between 2.70 and 7.00 K for the 400 μm channel, as described in the text. The straight line is a linear fit and the crosses are the error bars in the measured temperature and the measured signal.

1994ApJ...428..384L

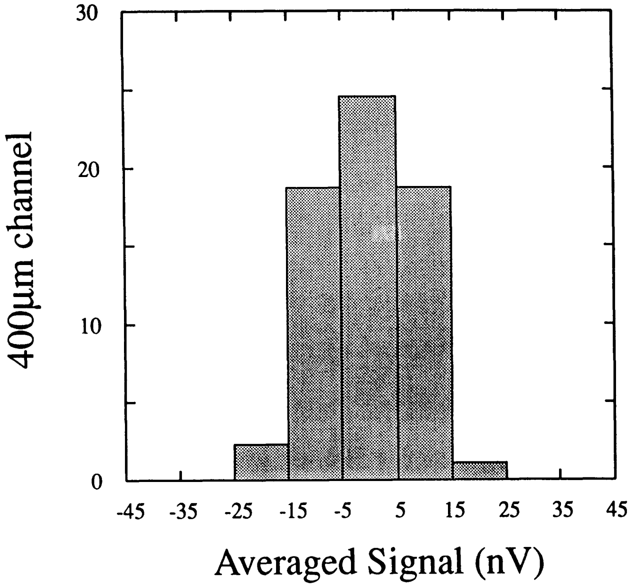

FIG. 7.—Histogram of the measured noise (in nV) of the shutter difference signal for the 400 μm channel, referred to the detector, after averaging over one shutter cycle.

black. The focal plane thus viewed a greybody with 0.3% of the throughput at the temperature of the blackbody, and the remainder of the throughput at approximately 2 K. The blackbody temperature was controlled at six temperatures between 5 and 18 K.

This calibration was flawed by a small temperature rise of the black front surface for blackbody temperatures above about 10 K. Because the front surface fills such a large solid angle relative to the warm blackbody, even a small temperature rise produces significant emission, particularly in the long-wavelength channels. The effects of the black front surface heating were modeled using the response of the 700 μm channel. The measured responsivity as a function of blackbody temperature after these effects are accounted for is shown in Figure 8. The responsivity is constant to within 5% for the three longer wavelength channels, for which the flux in band varies by more than two orders of magnitude. Larger deviations in the shortest wavelength channel are due to errors in spectroscopy, which underestimated the response at frequencies well below the passband. There is no evidence of any high-frequency leak in any of the passbands.

In a separate calibration experiment the IRTS telescope aperture was filled with a blackbody with a single blackbody temperature. The responsivity of the system measured in this calibration relative to that measured without the telescope is $\approx$30% lower, consistent with the obscuration due to the secondary mirror.

5.3. *Beam Pattern Measurements*

The beam pattern was measured by using a chopped thermal source which was collimated by a 50 cm Ritchy-Chretien telescope placed immediately in front of the IRTS. The collimating telescope was scanned in azimuth at several different altitude angles, in order to provide a two-dimensional map of the beam. The FIRP shutter was disabled in the open position during the measurement, so that only the collimated source was modulated. High signal-to-noise measurements could be obtained only for the longer wavelength channels, due to atmospheric absorption. The beam pattern of the 400 μm channel is shown in Figure 9. The beam has a FWHM of 0°.4, with 90% of the power contained within a diameter of 1 degree. Measurements for the other channels have lower signal noise to noise, but are consistent with the same pattern. The beams for the four channels are coincident with each other, as expected.

5.4. *Sensitivity*

The sensitivity of the FIRP depends on the responsivities determined by the laboratory calibration and the measured noise. Of all four focal plane instruments on the IRTS, the FIRP is observed to be most vulnerable to excess noise produced by electromagnetic interference. This is not surprising, considering that the intrinsic spectral noise density of the detectors and cooled preamplifiers is less than 20 nV $\mathrm{Hz}^{1/2}$, at least one order of magnitude less than any of the other instruments. The degree of electromagnetic interference has been greatly reduced by isolating the FIRP electrically from the rest of the focal plane, connecting the housing to detector ground, and by placing two-pole LC filters with a high-frequency cutoff at 100 kHz in each electrical line where it enters the housing. In

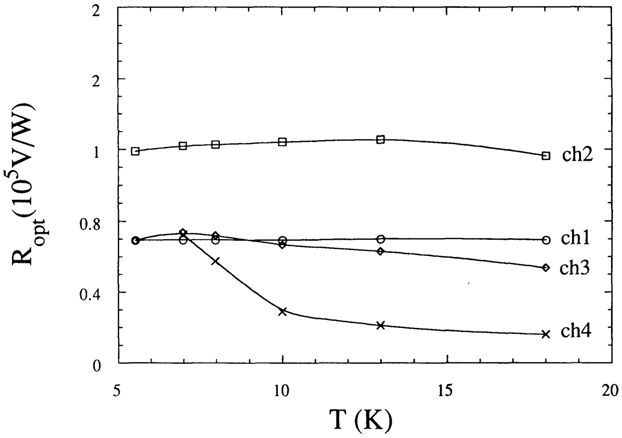

FIG. 8.—Results of the calibration in the telescope, as described in the text. R_{opt} is the optical responsivity accounting for the throughput of the intervening optics.

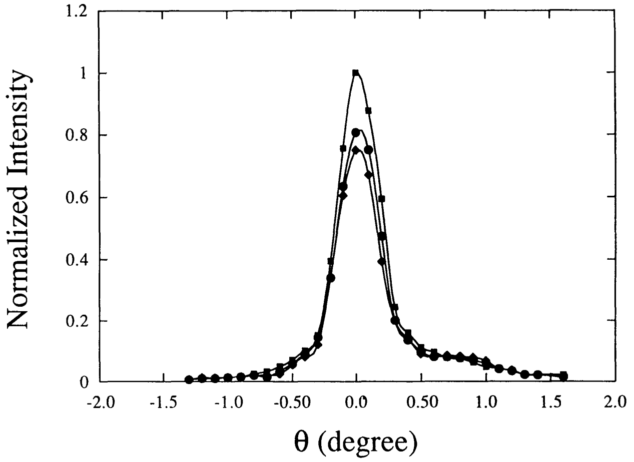

FIG. 9.—Measured beam pattern of the 400 μm channel. The squares indicate a scan through the center of the beam. The circles and the diamonds indicate scans displaced by ±0°.1 away from the center.

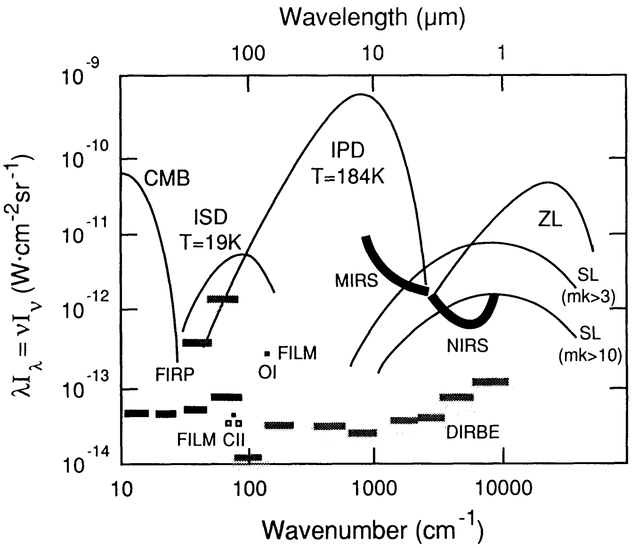

FIG. 10.—Sensitivity of the FIRP and the other three IRTS science instruments, compared with an estimate of the brightness of the diffuse background in a dark region of the sky. The different components are zodiacal light (ZL), thermal emission of the interplanetary dust (IPD) at 184 K and spectral index $n = 1$ (Hauser et al. 1984), integrated star light (SL), thermal emission from interstellar dust (ISD), and the 2.74 K cosmic background radiation (CMB). The two curves for integrated star light correspond to contributions from K-magnitude $m_k > 3$ and $m_k > 10$. The FIRP sensitivity is calculated from the laboratory measurements of responsivity and noise. Also indicated are the DIRBE sensitivities measured in flight. All values correspond to 1 σ/spectral element/field of view/mission (values for DIRBE are for a 1 year mission).

its present configuration, the variance of the average signals for each shutter cycle $\langle S_n \rangle$, is approximately 4 nV when all of the focal plane instruments are operating. The sensitivities of the four channels per pixel for this noise level are shown in Figure 10, assuming that each pixel is observed in eight passes. The sensitivities for the four channels are about 4×10^{-14}, 4×10^{-14}, 5×10^{-14}, and 9×10^{-14} W cm^{-2} sr^{-1}, respectively. Pixels near the ecliptic poles will be observed more often, with correspondingly higher sensitivity.

6. CONCLUSIONS

A Far-Infrared Photometer for the Infrared Telescope in Space has been constructed, tested, and calibrated in the laboratory. The FIRP will provide observations of the diffuse sub-mm background with unprecedented sensitivity and/or spatial resolution at wavelengths of 100 to 800 μm. No other orbital mission now being planned will provide observations of the diffuse continuum from 200 to 800 μm, a region which contains an important window on the extragalactic background. FIRP observations over a fraction of the sky will, when combined with the all-sky coverage of the FIRAS and DIRBE instruments on *COBE*, help constrain models of the ISD emission. An improved understanding at the long wavelength spectrum and distribution of ISD emissions will reduce the effects of confusion by ISD emission on measurements of CMB anisotropy, and on searches for the sub-mm extragalactic background. Eventually, the calibrated data sets from all four focal plane instruments will be made available to the public through the Infrared Processing and Analysis Center.

Many people at U.C. Berkeley contributed to the development of the FIRP, including undergraduates Gary Brubaker, Scott Chegwidden, Sabrina Grannan, Sim Larkin, Steve Lumetta, and Fred Rieke; engineering aid Brent Grossman; graduate students Dave Alsop, Jamie Bock, Mark Devlin, and Thor Wilbanks, and postdoctoral fellow Lionel Duband. Paul Richards was an active and invaluable participant in the early phases of this work. The Berkeley physics machine shop did an exceptional job in fabricating all of the mechanical components. Glenn Ecord at NASA/JSFC provided invaluable help in safety qualifying the ^{3}He refrigerator for the STS.

The development of the FIRP has been supported primarily through NASA grant NAGW-1527. We gratefully acknowledge the support for development of technologies that made the FIRP possible from the National Science Foundation/Astronomical Instrumentation Division through a PYI grant to A.E.L. and through a Research Opportunities for Undergraduates grant, from the Alfred P. Sloan Foundation, from the California Space Institute, and from NASA/AMES research consortium agreement NCA2-240. The integration of the FIRP into the IRTS was made possible in part by support from the Japan Society for the Promotion of Science in the form of a fellowship to M.M.F., and by support from the Japanese Institute of Space and Astronautical Science (ISAS) in the form of a Visiting Professorship for A.E.L. We especially thank Haruyuki Okuda, Hiroshi Murakami, Hiroshi Shibai, and other members of the ISAS staff and IRTS team for their kind support throughout this project.

REFERENCES

Ade, P. A. R., Griffin, M. J., Cunningham, C. T., Radostitz, J. V., Predko, S., & Nolt, I. G. 1984, Infrared Phys., 24, 403
Beichman, C. A., & Helou, G. 1990, ApJ, 370, L1
Bock, J., et al. 1993, ApJ, 410, 115
Bock, J., Lange, A. E., Matsuhara, H., Matsumoto, T., Onaka, T., & Sato, S. 1994, Appl. Opt., submitted
Boggess, N. W., et al. 1992, ApJ, 397, 420
Bond, J. R. 1989, in Frontiers in Physics—From Colliders to Cosmology, ed. A. Astbury et al. (Singapore: World Scientific), 182
Devlin, M., Lange, A. E., Wilbanks, T., & Sato, S. 1993, IEEE Trans. Nucl. Sci., 40, 162
Duband, L., Alsop, D., Lange, A. E., & Kittel, P. 1990a, Adv. Cryog. Eng., 35, 1447
Duband, L., Hui, L., & Lange, A. 1990b, Cryogenics, 30, 263
Duband, L., Alsop, D., Lange, A., Hayata, S., Matsumoto, T., & Sato, S. 1991, Cryogenics, 31, 338
———. 1993, Cryogenics, 33, 643
Fischer, M. L., et al. 1992, ApJ, 388, 242
Fischer, M. L., et al. 1994, ApJ, submitted
Gush, H. P., Halpern, M., & Wishnow, E. H. 1990, Phys. Rev. Lett., 65, 537
Hauser, M. G., et al. 1984, ApJ, 278, L15
Hauser, M. G., Kelsall, T., Moseley, S. H., Jr., Silverberg, R. F., Murdock, T., Toller, G., Spiesman, W., & Weiland, J. 1991, in After the First Three Minutes, ed. S. S. Holt et al. (New York: AIP), 161
Kawada, M., et al. 1993, ApJ, 425, 89
Lange, A. E., Hayakawa, S., Matsumoto, T., Matsuo, H., Murakami, H., Richards, P. L., & Sato, S. 1987, Appl. Opt., 26, 401
Lange, A. E., Kreysa, E., McBride, S. E., Richards, P. L., & Heller, E. E. 1983, Int. J. Infrared Millimeter Waves, 4, 689
Mather, J. C. 1984, Appl. Opt., 23, 584
Mather, J. C., et al. 1990, ApJ, 357, L37
Murakami, H., et al. 1994, ApJ, 428, 354
Noda, M., Matsumoto, T., Matsuura, S., Noguchi, K., Tanaka, M., & Lim, M. 1994, ApJ, 428, in press
Onaka, T., Yagi, T., Shibai, H., Kohno, T., Tanabe, T., & Murakami, H. 1994, ApJ,, submitted
Roellig, T., Onaka, T., McMahon, T. J., & Tanabe, T. 1994, ApJ, 428, 370
Shibai, H., Yui, M., Matsuhara, M., Hiromoto, N., Nakagawa, T., & Okuda, H. 1994, ApJ, 428, 377
Timusk, T., & Richards, P. L. 1981, Appl. Opt., 20, 1355
Wang, B. 1991, ApJ, 374, 465
Wilbanks, T., Devlin, M., Lange, A. E., Sato, S., Beeman, J. W., & Haller, E. E. 1990, IEEE Trans. Nucl. Sci., 37, 566
Winston, R. 1970, J. Opt. Soc. Am., 60, 245
Wright, E. L. 1987, ApJ, 320, 818
Wright, E. L., et al. 1991, ApJ, 381, 200
Yamada, Y., Mitsuishi, A., & Yoshinaga, H. 1962, J. Opt. Soc. Am., 52, 17